

# Exciton–polaron Umklapp scattering in Wigner crystals

Erfu Liu<sup>1,2†</sup>, Matthew Wilson<sup>1†</sup>, Jenny Hu<sup>3,4</sup>, Alexandra Zimmerman<sup>3,4</sup>, Amal Mathew<sup>3,4</sup>, Tianyi Ouyang<sup>1</sup>, Ao Shi<sup>1</sup>, Takashi Taniguchi<sup>5</sup>, Kenji Watanabe<sup>6</sup>, Tony F. Heinz<sup>3,4</sup>, Yia-Chung Chang<sup>7,8\*</sup> Chun Hung Lui<sup>1\*</sup>

<sup>1</sup>Department of Physics and Astronomy, University of California, Riverside, CA 92521, USA.

<sup>2</sup>School of Physics, National Laboratory of Solid State Microstructures, and Collaborative Innovation Center for Advanced Microstructures, Nanjing University, Nanjing, China.

<sup>3</sup>Department of Applied Physics, Stanford University, Stanford, CA 94305, USA

<sup>4</sup>SLAC National Accelerator Laboratory, Menlo Park, CA 94025, USA

<sup>5</sup>Research Center for Materials Nanoarchitectonics, National Institute for Materials Science, 1–1 Namiki, Tsukuba 305–0044, Japan

<sup>6</sup>Research Center for Electronic and Optical Materials, National Institute for Materials Science, 1–1 Namiki, Tsukuba 305–0044, Japan

<sup>7</sup>Research Center for Applied Sciences, Academia Sinica, Taipei 11529, Taiwan

<sup>8</sup>Department of Physics, National Cheng Kung University, Tainan, 701 Taiwan

† These authors contributed equally to the work.

\*Corresponding author. Email: [yiachang@gate.sinica.edu.tw](mailto:yiachang@gate.sinica.edu.tw); [joshua.lui@ucr.edu](mailto:joshua.lui@ucr.edu)

## Abstract:

Strong Coulomb interactions in two-dimensional (2D) semiconductors give rise to tightly bound excitons, exciton polarons, and correlated electronic phases such as Wigner crystals (WCs), yet their mutual interplay remains poorly understood. Here we report the observation of multi-branch excitonic Umklapp scattering in both electron and hole WCs realized in ultraclean monolayer WSe<sub>2</sub>, exhibiting exceptionally high melting temperatures ( $T_c \approx 20$ –30 K). Robust Wigner crystallization activates multiple finite-momentum optical resonances, including quasilinearly dispersing, light-like excitons and exciton polarons, extending far beyond the single excitonic Umklapp feature reported previously. Helicity-resolved magneto-optical measurements reveal a pronounced valley dependence of the scattering processes. Combined experiment and theory identify a polaron-induced brightening mechanism in which exciton polarons transfer oscillator strength from bright zero-momentum states to otherwise dark finite-momentum states, explaining the emergence of multiple Umklapp branches where conventional exciton–WC scattering is ineffective. These results establish WC polarons as a new quasiparticle paradigm and introduce polaron-induced Umklapp scattering as a general route to accessing finite-momentum many-body excitations in 2D quantum materials.

Polarons—quasiparticles formed when an excitation is dressed by collective many-body degrees of freedom—are a cornerstone of condensed-matter physics<sup>1-4</sup>. In atomically thin semiconductors, exciton polarons have emerged as a powerful framework for interpreting optical spectra in the presence of itinerant charge carriers, where excitons are dressed by a polarized Fermi sea<sup>5-10</sup>. Despite this progress, all exciton polarons explored experimentally to date share a defining characteristic: the dressing medium is a liquid. How polaron physics evolves when the electronic environment instead crystallizes into a strongly correlated Wigner crystal (WC) remains an open and largely unexplored question.

Wigner crystals represent the extreme limit of Coulomb-dominated electronic correlations, in which electrons or holes self-organize into an ordered lattice (Fig. 1A). This crystalline order breaks continuous translational symmetry and introduces a discrete set of lattice vectors in reciprocal space<sup>11-20</sup>. Recent optical studies in atomically thin semiconductors have shown that such charge lattices can weakly scatter excitons<sup>13, 17</sup>, enabling Umklapp processes that activate otherwise dark finite-momentum states (Fig. 1B). However, these observations were interpreted within a predominantly excitonic framework and were limited to a single Umklapp feature associated with quadratically dispersing excitons on the electron-doped side<sup>13, 17</sup>. Whether Wigner crystallization qualitatively reshapes polaron physics—and whether it can give rise to fundamentally new optical activation mechanisms beyond conventional exciton-WC scattering—has remained unknown.

In this Article, we demonstrate that the WC regime in a two-dimensional (2D) semiconductor gives rise to a new form of Umklapp scattering governed by many-body polaron dressing. Using ultraclean monolayer WSe<sub>2</sub> devices, we realize WCs of both electrons and holes, with unusually high melting temperatures ( $T_c \approx 20-30$  K), enabling direct comparison of Umklapp processes on the two sides of charge neutrality. In the WC regime, we observe multiple Umklapp branches, far exceeding the single exciton Umklapp line reported previously. These include not only quadratically dispersing excitons but also quasilinearly dispersing, light-like excitons and exciton polarons, revealing a much richer finite-momentum excitation spectrum than previously accessible (Fig. 1B-C). Helicity-resolved magneto-optical measurements further uncover a pronounced valley dependence of Umklapp scattering, reflecting the role of exchange interactions between excitons and the WC. Umklapp processes are strongly enhanced on the hole-doped side when excitons and WCs occupy the same valley and electronic band, while otherwise remaining weak.

Crucially, the observed multiplicity of Umklapp branches — particularly on the electron-doped side — cannot be explained by excitonic Umklapp scattering alone. Instead, it originates from a polaron-induced brightening mechanism in which exciton polarons transfer oscillator strength from bright zero-momentum states to otherwise dark finite-momentum Umklapp states. These results establish WC polarons as a new quasiparticle paradigm and show that electronic crystallization can effectively relax optical selection rules via Umklapp processes in 2D quantum materials.

## Umklapp scattering of quasilinearly dispersing excitons and exciton polarons

Our experiments employ single-gate monolayer WSe<sub>2</sub> devices encapsulated in hexagonal boron nitride (BN), with thin graphite serving as contact and gate electrodes (Fig. 2A). A gate voltage  $V_g$  is applied to inject electrons or holes into the WSe<sub>2</sub> monolayer. We measure reflection spectra  $R_s$  from WSe<sub>2</sub> and reference spectra  $R_r$  from a nearby area without WSe<sub>2</sub> to obtain the reflectance contrast, defined as  $\Delta R/R = (R_s - R_r)/R_r$ . Fig. 2B displays a gate-dependent  $\Delta R/R$  map of Device 1, which exhibits the  $A^0$  exciton and its exciton polarons on the electron ( $A_1^-, A_2^-$ ) and hole ( $A^+$ ) sides<sup>8, 21, 22</sup>. A gate-dependent  $\Delta R/R$  trace near 1.72 eV (black arrows and overlying spectrum in Fig. 2B) reveals two features ( $A_{eu2}^0, A_{hu2}^0$ ), indicating additional states. To enhance the visibility of these weak features, we calculate the second derivative of the spectra with respect to photon energy. The resulting second-derivative  $\Delta R/R$  map (Fig. 2C) then reveals five weak lines, namely, the  $A_{hu1}^0$  and  $A_{hu2}^0$  lines on the hole side, the  $A_{eu2}^0$  line on the electron side, and the  $A_{1u}^-$  and  $A_{2u}^-$  lines above the exciton polarons on the electron side. We evaluate the energy spacings ( $\Delta E$ ) between the  $A_{eu2}^0, A_{hu2}^0, A_{hu1}^0$  lines and the primary  $A^0$  line. The  $\Delta E$  values increase nearly linearly with the density of the injected carriers (Fig. 2D). Similar results have been observed in two additional devices (Figs. S3, S4).

Prior studies on monolayer MoSe<sub>2</sub> reported a similar weak Umklapp line for excitons on the electron side, attributed to the Umklapp scattering of quadratically dispersing excitons due to the presence of a WC<sup>13</sup>. Following a similar approach, we compare our results with the calculated density-dependent energy of the Umklapp state using an effective exciton mass of  $0.8m_e$  for monolayer WSe<sub>2</sub> (black lines in Fig. 2D). We find good agreement between the quadratic dispersion and the  $A_{hu1}^0$  line, confirming the presence of WC in our sample.

In contrast, the  $A_{hu2}^0$  and  $A_{eu2}^0$  lines lie well above the energies of the quadratically dispersing exciton, indicating the presence of an additional exciton branch. Theory has predicted that excitons in the K and K' valleys can couple via electron–hole (e–h) exchange interactions, giving rise to two branches with quadratic and quasilinear dispersions<sup>23–25</sup>, consistent with recent experiments<sup>26, 27</sup>. Figure 1B shows these double exciton branches in monolayer WSe<sub>2</sub> from our calculations (see Supplementary Section II.6.2 for details). The linear component of the quasilinear branch arises from intra- and intervalley e–h exchange interactions characterized by a common strength  $J$ . Figure 2D shows the calculated energy positions of the Umklapp lines associated with this branch. Using  $J = 160$  and  $180$  meV, we obtain good agreement with the observed  $A_{hu2}^0$  and  $A_{eu2}^0$  lines, respectively, confirming their origin from the quasilinear exciton branch.

In addition, we observe previously unreported Umklapp lines ( $A_{1u}^-, A_{2u}^-$ ) associated with the  $A_1^-$  and  $A_2^-$  exciton polaron. Unlike the  $A^0$  exciton with two Umklapp lines, each exciton polaron shows only a single Umklapp line, indicating a single exciton–polaron branch. This behavior arises because exciton polarons in opposite valleys are dressed by distinct Fermi seas. Since their many-body dressing clouds are different, the corresponding exciton–polaron wavefunctions have zero overlap, preventing any coupling between polarons from opposite valleys. Consequently, exciton

polarons experience only intravalley e–h exchange interactions. This leads to a single quasilinear dispersion branch with a linear component approximately half that of the  $A^0$  exciton, as illustrated in Fig. 1C.

## Robustness of Wigner crystals at elevated density and temperature

Wigner crystals are known as delicate correlated states, which stabilize only at low carrier densities and temperatures<sup>28–37</sup>. Prior theory established that an ideal 2D electron system can only form a WC at low density with a Wigner–Seitz radius  $r_s > 31$ <sup>18, 38</sup>. Yet the Umklapp scattering signals in our data (Fig. 2C–D) persist up to a hole density of  $1 \times 10^{12} \text{ cm}^{-2}$ , corresponding to  $r_s \sim 10$ , well below the theoretical threshold (see Supplementary Section I.6 for details). This apparent breakdown of the theoretical limit hints that lattice defects might help stabilize the WC formation in monolayer WSe<sub>2</sub><sup>15–17</sup>.

To evaluate the WC robustness against thermal fluctuations, Fig. 2E displays the integrated intensity of the  $A_{eu2}^0$ ,  $A_{hu2}^0$  lines as a function of temperature. Both Umklapp lines diminish with increasing temperature and disappear at critical temperatures of approximately  $T_c = 27 \text{ K}$  and  $21 \text{ K}$  on the electron and hole sides, respectively. Since our setup measures only the cold–finger temperature, the sample temperature should be several degrees higher, implying a WC melting temperature near  $30 \text{ K}$ . This value well exceeds the  $T_c \sim 11 \text{ K}$  reported for monolayer MoSe<sub>2</sub><sup>13</sup>. Both the low Wigner–Seitz radius  $r_s$  and high melting temperature  $T_c$  indicate monolayer WSe<sub>2</sub> as an excellent WC platform.

## Umklapp scattering due to exciton–WC scattering

Next, we investigate the physical mechanisms of the observed Umklapp scattering processes with WCs. To this end, we conduct helicity–resolved optical measurements under a vertical magnetic field  $B = 17 \text{ T}$  that lifts the valley degeneracy (Fig. 3A–B). Optical helicity enables selective probing of the  $K$  or  $K'$  valley, while the injection of electrons or holes enables selective population of these valleys<sup>39–42</sup>. The interplay of these factors reveals four distinct exciton–WC scenarios, as illustrated in the right column of Fig. 3 at vertical positions corresponding to the map sections in Fig. 3A–B. In Case 1, both the exciton and WC reside in the  $K'$  valley but occupy different bands. In Case 2, the exciton resides in the  $K'$  valley, while a hole WC occupies the  $K$  valley. In Case 3, the exciton resides in the  $K$  valley, while an electron WC resides in the  $K'$  valley. In Case 4, both the exciton and hole WC reside in the  $K$  valley. A crucial distinction arises in Case 4, where the hole in the exciton resides in the same band as the hole WC, unlike in Cases 1–3 where excitons and WCs are associated with different bands.

Fig. 3A–B reveal a striking feature—the Umklapp line in Case 4 is much brighter than those in Cases 1–3. To understand this distinction, we need to know that an exciton, being charge–neutral, has near–zero net direct Coulomb interaction with the WC, because its electron and hole

components exhibit opposite scattering amplitudes that largely cancel each other out. Therefore, the exciton–WC scattering depends crucially on the exchange interactions, where Cases 1–3 and Case 4 exhibit distinct behavior. In Cases 1–3, the exciton and WC occupy different bands, leading to negligible exciton–WC exchange interaction; as a result, the overall exciton–WC scattering is weak (Fig. 3F). In Case 4, by contrast, the hole of the exciton occupies the same band as the hole WC, leading to a strong long–range exchange interaction between them due to Pauli exclusion, whereas the electron of the exciton occupies a different band with negligible exchange interaction with the hole WC. The uncompensated hole–WC and electron–WC exchange interaction leads to a strong net exciton–WC scattering effect.

To corroborate the picture above, we have calculated the exciton–WC scattering strength in all four cases, incorporating both long–range and short–range, direct and exchange Coulomb interactions. As shown in the left panel of Fig. 3E, the calculated scattering strength in Case 4 is one to two orders of magnitude greater than in Cases 1–3, consistent with our experimental observation in Fig. 3A–B. Using this exciton–WC scattering model, we further simulate an optical conductivity map at zero magnetic field for excitons in monolayer WSe<sub>2</sub> (Fig. 4A). Our simulation includes both the quadratic and quasilinear exciton branches, producing two Umklapp lines that match the observed  $A_{hu1}^0$  and  $A_{hu2}^0$  lines.

While our simulation in Fig. 4A accounts well for the exciton Umklapp lines on the hole side, it produces negligible Umklapp lines on the electron side because of the weak exciton–WC scattering in Cases 1 and 2 (Fig. 3E). Similarly weak optical response is expected for polaron–WC scattering, as it primarily involves the excitonic component of the polaron hopping across different WC sites. Yet our experiment observes not only a pronounced exciton Umklapp line ( $A_{eu2}^0$ ) but also two exciton–polaron Umklapp lines ( $A_{1u}^-$ ,  $A_{2u}^-$ ) on the electron side. These deviations point to an alternative mechanism—likely involving polaron effects—that governs Umklapp scattering on the electron side.

## Umklapp scattering due to exciton–polaron effect

We construct a polaron model to elucidate the role of exciton–polaron coupling in Umklapp scattering (see Supplementary Section II.7 for details). For clarity, we illustrate our model on the hole–doped regime with only a single exciton polaron. The model includes five basis states: the primary exciton  $|X_{s=0}^K\rangle_R$ , the primary tetron  $|\mathfrak{I}_{s=0}\rangle_R$  and its Umklapp counterpart  $|\mathfrak{I}_{s=1}\rangle_R$ , as well as two Umklapp excitons  $|X_{s=1}^K\rangle_R$  and  $|X_{s=1}^{K'}\rangle_R$ . Here, a tetron refers to an exciton bound to a WC charge, forming a localized trion with an accompanying WC vacancy (Fig. 1A); unlike conventional tetrons defined by Fermi–sea dressing of an exciton, these tetrons arise from distortions of the WC<sup>6, 43, 44</sup>. All states are associated with the  $K$  valley except  $|X_{s=1}^{K'}\rangle_R$ , which belongs to the  $K'$  valley, and the subscript R denotes right–handed optical helicity. The index  $s = 0$  labels the zeroth star in the group theory, corresponding to zero–momentum excitations, whereas

$s = 1$  labels the first stars, corresponding to a linear combination of six Umklapp states at the first set of WC reciprocal lattice vectors. The presence of the WC enables coupling between the  $s = 0$  and  $s = 1$  states, facilitating polaron-mediated interactions.

Using these basis states, we construct the Hamiltonian:

$$\begin{pmatrix} E_0^X & U_{X\Im}^{00} & U_{X\Im}^{01} & 0 & 0 \\ U_{X\Im}^{00} & E_0^{\Im} & 0 & U_{X\Im}^{10} & 0 \\ U_{X\Im}^{01} & 0 & E_1^{\Im} + \frac{Jg_1}{K} & U_{X\Im}^{11} & 0 \\ 0 & U_{X\Im}^{10} & U_{X\Im}^{11} & E_1^X + \frac{Jg_1}{K} & \frac{Jg_1}{K} \\ 0 & 0 & 0 & \frac{Jg_1}{K} & E_1^X + \frac{Jg_1}{K} \end{pmatrix} \begin{pmatrix} C_{0R}^K \\ C_{0R}^{\Im} \\ C_{1R}^{\Im} \\ C_{1R}^K \\ C_{1R}^{K'} \end{pmatrix} = E_P \begin{pmatrix} C_{0R}^K \\ C_{0R}^{\Im} \\ C_{1R}^{\Im} \\ C_{1R}^K \\ C_{1R}^{K'} \end{pmatrix} \quad (1)$$

Here, the  $C$ 's are the expansion coefficients and  $E_P$  denotes the eigenenergies. The parameters  $J$ ,  $g_1$ , and  $K$  represent the e–h exchange interaction strength, the magnitude of the WC reciprocal lattice vector, and the momentum magnitude at the K point, respectively. The  $Jg_1/K$  terms modulate and couple the two Umklapp excitons  $|X_{s=1}^K\rangle_R$  and  $|X_{s=1}^{K'}\rangle_R$ , producing the two excitonic branches shown in Fig. 1B.

A key feature of Eq. (1) is the presence of off-diagonal terms  $U_{X\Im}$ , which hybridize the exciton and tetron states. Among the basic states, only the primary exciton and tetron are optically bright, while the Umklapp states are all initially dark. However, solving Eq. (1) reveals new eigenstates formed as linear combinations of the basis functions, where the Umklapp states become optically active due to mixing with the primary states. This mixing is mediated by the polaron effect, driven by the  $U_{X\Im}$  coupling terms. An analogous Hamiltonian with seven basis states can be constructed for the electron-doped regime, where two tetrons are involved.

Fig. 4B displays the optical conductivity map calculated using this model, which includes the polaron effect but not the exciton–WC scattering effect. The theoretical map exhibits two Umklapp lines for each exciton and one Umklapp line for each polaron. A comparison of Fig. 4A, which includes exciton–WC scattering but no polaron effect, and Fig. 4B, which includes the polaron effect but no exciton–WC scattering, reveals complementary behaviors. While the  $A_{hu1}^0$  and  $A_{hu2}^0$  lines are strong in Fig. 4A, they are weak in Fig. 4B. This is because Case 4 exhibits strong exciton–WC scattering but no polaron effect, as the hole occupies the same band as the WC, whereas Cases 1–3 exhibit weak exciton–WC scattering but strong polaron effect because the exciton occupies different bands from the WC.

## Simulations with both exciton–WC scattering and exciton–polaron effects

After treating the exciton–WC scattering and exciton–polaron effects separately, we combine their contributions incoherently—assuming that lattice defects and valley disorder of the WC sites destroy any phase coherence between the two—to obtain the total optical conductivity map shown

in Fig. 4C (see Supplementary Section II.8 for details). Afterward, we calculate the reflectance contrast spectra by solving the optical interference problem in our device geometry. We also broaden the spectral lines, add a background to account for states outside our energy range, and perform a second-order energy derivative to highlight the weak features. The resulting simulated  $d^2(\Delta R/R)/dE^2$  map, as shown in Fig. 2F, shows good agreement with our experimental map in Fig. 2C.

We further calculated the Umklapp states under a magnetic field, which generates distinct Zeeman shifts on different Umklapp states by lifting the valley degeneracy (see Supplementary Section II.9 for details). Fig. 3C–D displays the simulated  $d^2(\Delta R/R)/dE^2$  maps at  $B = 17$  T, which agree reasonably with experiment. The simulation–experiment comparison allows us to identify the observed weaker lines in Fig. 3A–B as the  $A_{eu2}^0$  and  $A_{hu2}^0$  lines and the strong line as the  $A_{hu1}^0$  line.

In summary, we uncover a previously inaccessible regime of Umklapp physics in 2D Wigner crystals (WCs), in which polaron effects play a central role. The emergence of multiple Umklapp features—encompassing both excitonic and polaronic excitations with unconventional dispersion—reveals a brightening mechanism whereby many-body interactions redistribute optical strength rather than simply providing momentum. Such behavior lies beyond a single-particle exciton description and underscores the importance of polaron formation in a crystalline electronic environment. Our results identify WC polarons as a distinct class of correlated quasiparticles. More broadly, these findings establish Umklapp processes as a powerful tool for probing and controlling finite-momentum excitations, with implications for interaction–driven phases, valley–selective effects, and nonequilibrium phenomena in 2D quantum materials.

During the preparation of our manuscript, we became aware of related works from other groups<sup>45–47</sup>.

## References:

1. Schirotzek, A., Wu, C.-H., Sommer, A. & Zwierlein, M.W. Observation of Fermi Polarons in a Tunable Fermi Liquid of Ultracold Atoms. *Phys. Rev. Lett.* **102**, 230402 (2009).
2. Koschorreck, M. et al. Attractive and repulsive Fermi polarons in two dimensions. *Nature* **485**, 619–622 (2012).
3. Kohstall, C. et al. Metastability and coherence of repulsive polarons in a strongly interacting Fermi mixture. *Nature* **485**, 615–618 (2012).
4. Schmidt, R., Enss, T., Pietilä, V. & Demler, E. Fermi polarons in two dimensions. *Phys. Rev. A* **85**, 021602 (2012).
5. Efimkin, D.K. & MacDonald, A.H. Many-body theory of trion absorption features in two-dimensional semiconductors. *Phys. Rev. B* **95**, 035417 (2017).
6. Chang, Y.-C., Shiau, S.-Y. & Combescot, M. Crossover from trion-hole complex to exciton-polaron in n-doped two-dimensional semiconductor quantum wells. *Phys. Rev. B* **98**, 235203

(2018).

7. Efimkin, D.K. & MacDonald, A.H. Exciton-polarons in doped semiconductors in a strong magnetic field. *Phys. Rev. B* **97**, 235432 (2018).
8. Liu, E. et al. Exciton-polaron Rydberg states in monolayer MoSe<sub>2</sub> and WSe<sub>2</sub>. *Nature Commun.* **12**, 6131 (2021).
9. Sidler, M. et al. Fermi polaron-polaritons in charge-tunable atomically thin semiconductors. *Nature Phys.* **13**, 255 (2017).
10. Fey, C., Schmelcher, P., Imamoglu, A. & Schmidt, R. Theory of exciton-electron scattering in atomically thin semiconductors. *Phys. Rev. B* **101**, 195417 (2020).
11. Wigner, E. On the Interaction of Electrons in Metals. *Phys. Rev.* **46**, 1002–1011 (1934).
12. Knörzer, J. et al. Wigner crystals in two-dimensional transition-metal dichalcogenides: Spin physics and readout. *Phys. Rev. B* **101**, 125101 (2020).
13. Smołński, T. et al. Signatures of Wigner crystal of electrons in a monolayer semiconductor. *Nature* **595**, 53–57 (2021).
14. Zhou, Y. et al. Bilayer Wigner crystals in a transition metal dichalcogenide heterostructure. *Nature* **595**, 48–52 (2021).
15. Xiang, Z. et al. Imaging quantum melting in a disordered 2D Wigner solid. *Science* **388**, 736–740 (2025).
16. Ge, Z. et al. arXiv:2510.12009 (2025).
17. Sung, J. et al. An electronic microemulsion phase emerging from a quantum crystal-to-liquid transition. *Nature Phys.* **21**, 437–443 (2025).
18. Zarenia, M., Neilson, D., Partoens, B. & Peeters, F.M. Wigner crystallization in transition metal dichalcogenides: A new approach to correlation energy. *Phys. Rev. B* **95**, 115438 (2017).
19. Brem, S. & Malic, E. Terahertz Fingerprint of Monolayer Wigner Crystals. *Nano Lett.* **22**, 1311–1315 (2022).
20. Shayegan, M. Wigner crystals in flat band 2D electron systems. *Nature Reviews Physics* **4**, 212–213 (2022).
21. Jones, A.M. et al. Optical generation of excitonic valley coherence in monolayer WSe<sub>2</sub>. *Nature Nanotech.* **8**, 634 (2013).
22. Courtade, E. et al. Charged excitons in monolayer WSe<sub>2</sub>: Experiment and theory. *Phys. Rev. B* **96**, 085302 (2017).
23. Yu, H., Liu, G.-B., Gong, P., Xu, X. & Yao, W. Dirac cones and Dirac saddle points of bright excitons in monolayer transition metal dichalcogenides. *Nature Commun.* **5**, 3876 (2014).
24. Qiu, D.Y., Cao, T. & Louie, S.G. Nonanalyticity, Valley Quantum Phases, and Lightlike Exciton Dispersion in Monolayer Transition Metal Dichalcogenides: Theory and First-Principles Calculations. *Phys. Rev. Lett.* **115**, 176801 (2015).
25. Wu, F., Qu, F. & MacDonald, A.H. Exciton band structure of monolayer MoS<sub>2</sub>. *Phys. Rev. B* **91**, 075310 (2015).
26. Liu, L.Y. et al. arXiv:2502.20454 (2025).
27. Delhomme, A. et al. arXiv:2508.13784 (2025).

28. Grimes, C.C. & Adams, G. Evidence for a Liquid-to-Crystal Phase Transition in a Classical, Two-Dimensional Sheet of Electrons. *Phys. Rev. Lett.* **42**, 795–798 (1979).

29. Andrei, E.Y. et al. Observation of a magnetically induced Wigner solid. *Phys. Rev. Lett.* **60**, 2765–2768 (1988).

30. Goldman, V.J., Santos, M., Shayegan, M. & Cunningham, J.E. Evidence for two-dimensional quantum Wigner crystal. *Phys. Rev. Lett.* **65**, 2189–2192 (1990).

31. Buhmann, H. et al. Novel magneto-optical behavior in the Wigner-solid regime. *Phys. Rev. Lett.* **66**, 926–929 (1991).

32. Chen, Y.P. et al. Melting of a 2D quantum electron solid in high magnetic field. *Nature Phys.* **2**, 452–455 (2006).

33. Tiemann, L., Rhone, T.D., Shibata, N. & Muraki, K. NMR profiling of quantum electron solids in high magnetic fields. *Nature Phys.* **10**, 648–652 (2014).

34. Deng, H. et al. Probing the Melting of a Two-Dimensional Quantum Wigner Crystal via its Screening Efficiency. *Phys. Rev. Lett.* **122**, 116601 (2019).

35. Deshpande, V.V. & Bockrath, M. The one-dimensional Wigner crystal in carbon nanotubes. *Nature Phys.* **4**, 314–318 (2008).

36. Shapir, I. et al. Imaging the electronic Wigner crystal in one dimension. *Science* **364**, 870–875 (2019).

37. Pecker, S. et al. Observation and spectroscopy of a two-electron Wigner molecule in an ultraclean carbon nanotube. *Nature Phys.* **9**, 576–581 (2013).

38. Drummond, N.D. & Needs, R.J. Phase Diagram of the Low-Density Two-Dimensional Homogeneous Electron Gas. *Phys. Rev. Lett.* **102**, 126402 (2009).

39. Li, Y. et al. Valley splitting and polarization by the Zeeman effect in monolayer MoSe<sub>2</sub>. *Phys. Rev. Lett.* **113**, 266804 (2014).

40. Aivazian, G. et al. Magnetic control of valley pseudospin in monolayer WSe<sub>2</sub>. *Nature Phys.* **11**, 148–152 (2015).

41. MacNeill, D. et al. Breaking of valley degeneracy by magnetic field in monolayer MoSe<sub>2</sub>. *Phys. Rev. Lett.* **114**, 037401 (2015).

42. Srivastava, A. et al. Valley Zeeman effect in elementary optical excitations of monolayer WSe<sub>2</sub>. *Nature Phys.* **11**, 141–147 (2015).

43. Ossau, W.J. & Suris, R. Optical properties of 2D systems with interacting electrons, Vol. 119. (Springer Science & Business Media, 2003).

44. Koudinov, A.V. et al. Suris tetrons: Possible spectroscopic evidence for four-particle optical excitations of a two-dimensional electron gas. *Phys. Rev. Lett.* **112**, 147402 (2014).

45. Wang, L. et al. arXiv:2512.16552 (2025).

46. Adlong, H.S., Dizer, E., Schmidt, R., Imamoglu, A. & Christianen, A. arXiv:2512.16651 (2025).

47. Zhang, L. et al. arXiv:2512.16631 (2025).

**Acknowledgment:** We thank S. A. McGill for assistance in the magneto-optical experiments and H. W. K. Tom for equipment support. C.H.L. acknowledges support from the National Science Foundation (NSF) Division of Materials Research CAREER Award No.1945660 and the American Chemical Society Petroleum Research Fund No. 61640-ND6. Y.C.C. is supported by the National Science and Technology Council (Taiwan) under grant Nos. NSTC 112-2112-M-001-054-MY2 and 114-2112-M-006-030. E.L. acknowledges support from the National Key R&D Program of China (grant no. 2024YFA1410500), the Fundamental Research Funds for the Central Universities, the National Natural Science Foundation of China (grant no. 12374456), the Program for Innovative Talents and Entrepreneur in Jiangsu, and the Jiangsu Provincial Department of Science and Technology (Grant No. BK20253040). Optical spectroscopy at SLAC/Stanford was supported by the Department of Energy, Office of Basic Energy Sciences, Division of Materials Sciences and Engineering under contract DE-AC02-76SF00515 (T.F.H., J. H., A. M. and A. Z.), with additional support for T.F.H. from the Gordon and Betty Moore Foundation EPiQS Initiative through grant no. GBMF9462. J.H. acknowledges support from an NTT Research Fellowship, and A. Z. acknowledges support from the National Science Foundation Graduate Research Fellowship Program under grant no. DGE-2146755. K.W. and T.T. acknowledge support from the JSPS KAKENHI (Grant Numbers 21H05233 and 23H02052), the CREST (JPMJCR24A5), JST and World Premier International Research Center Initiative (WPI), MEXT, Japan. A portion of this work was performed at the National High Magnetic Field Laboratory, which is supported by the National Science Foundation Cooperative Agreement No. DMR-1644779 and the State of Florida.

**Author contributions:** E.L. fabricated the devices. E.L., M.W., J.H., A.Z., A.M., T.O. and A.S. performed the experiments. M.W. and E.L. analyzed the data. T.T. and K.W. provided boron nitride crystals for device fabrication. T.F.H. supervised the research of J.H., A.Z., and A.M.. Y.C.C. performed the theoretical calculations. C.H.L. supervised the research and coordinated the work. C.H.L., Y.C.C. and M.W. wrote the manuscript.

**Competing interests:** The authors declare no competing interests.

#### **Additional information**

**Supplementary information** is available for this paper.

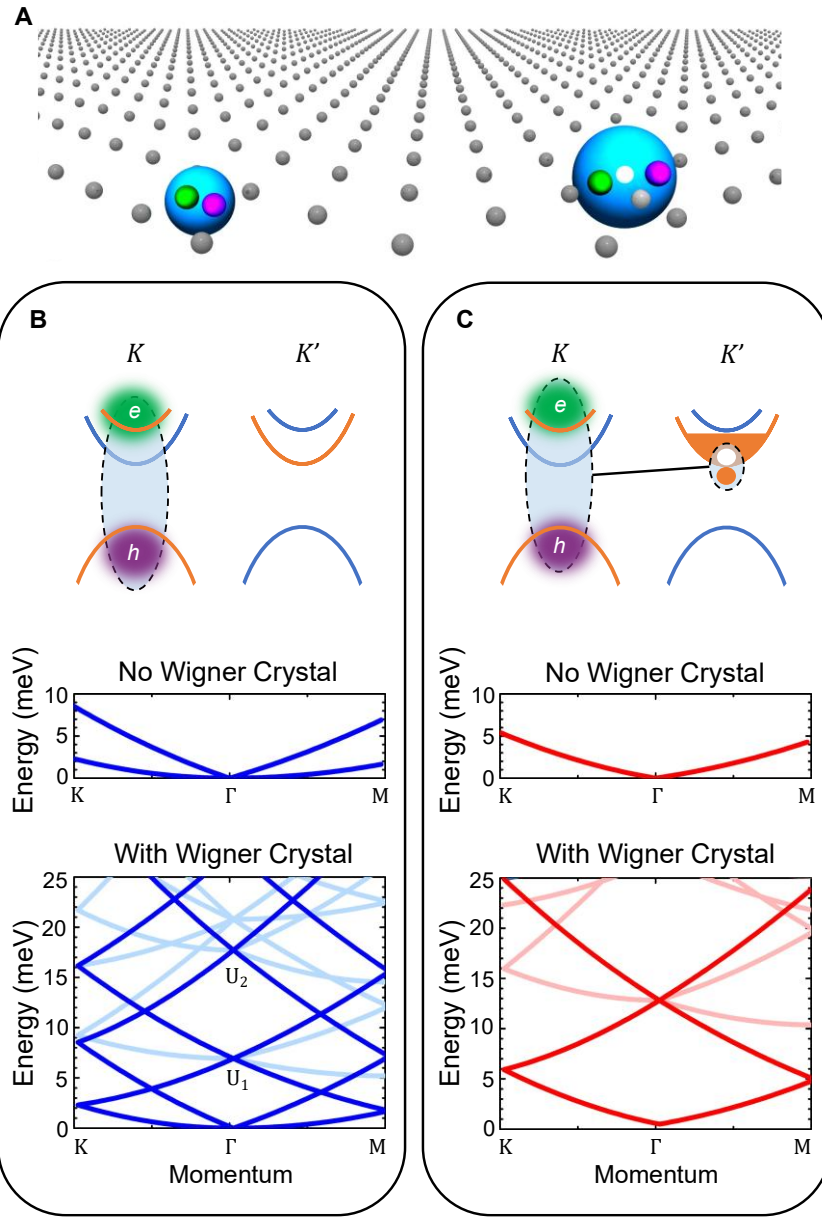


**Figure 1. Umklapp brightening of finite-momentum excitons and exciton polarons by a Wigner crystal.** (A) Schematic illustration of an exciton and an exciton polaron in a Wigner crystal (WC). The polaron consists of an exciton bound to a WC charge, accompanied by a corresponding WC vacancy. (B) Schematic illustration and dispersion of excitons in monolayer WSe<sub>2</sub>. Excitonic states from opposite valleys hybridize to form two branches with quadratic and quasilinear dispersions as functions of the center-of-mass (CM) wave vector. The WC induces a zone-folding effect. (C) Schematic illustration and dispersion of the exciton polaron. Because exciton polarons in opposite valleys do not couple owing to their distinct Fermi seas, they exhibit a single branch with quasilinear dispersion.

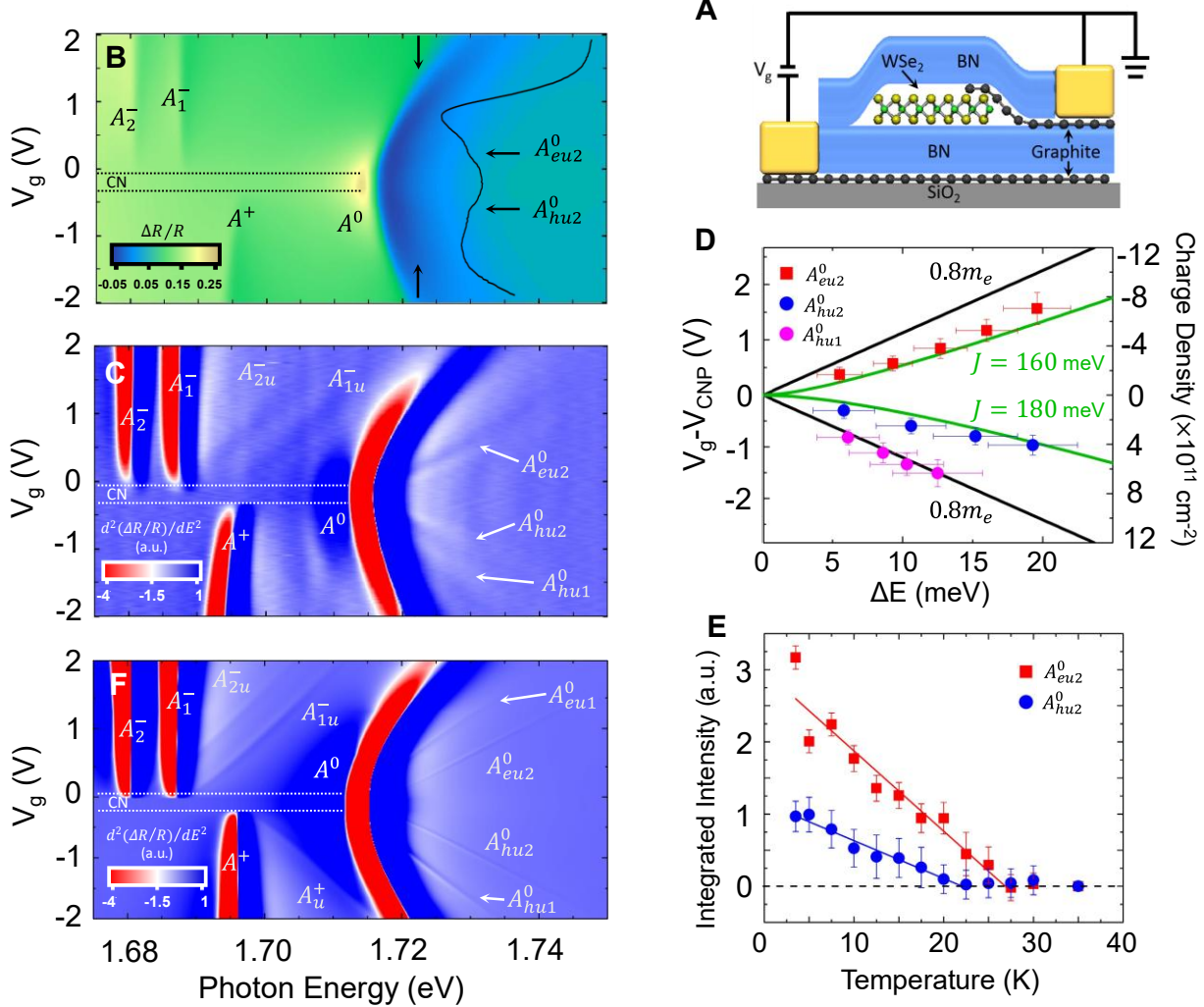


**Figure 2. Excitonic Umklapp scattering in electron and hole Wigner crystals in monolayer WSe<sub>2</sub>.** **(A)** Schematic of a monolayer WSe<sub>2</sub> device. **(B)** Gate-dependent reflectance contrast ( $\Delta R/R$ ) color map measured at  $T = 3.5$  K, showing the  $A^0$  exciton and  $A^+$ ,  $A_1^-$ ,  $A_2^-$  exciton polarons. The black trace denotes a gate-dependent profile at 1.722 eV (indicated by arrows), where two weak minima ( $A_{eu2}^0$ ,  $A_{hu2}^0$ ) mark the formation of electron and hole Wigner crystals. **(C)** Second-order energy derivative of the reflectance contrast map in panel B,  $d^2(\Delta R/R)/dE^2$ , highlighting multiple Umklapp spectral features. **(D)** Energy separation  $\Delta E$  between the  $A^0$  resonance and the  $A_{eu2}^0$ ,  $A_{hu1}^0$ , and  $A_{hu2}^0$  Umklapp features. The black (green) lines are the theoretical Umklapp positions based on the quadratic (quasilinear) exciton dispersion. **(E)** Temperature dependence of the Umklapp scattering signal intensity. **(F)** Simulated second-derivative reflectance contrast map.

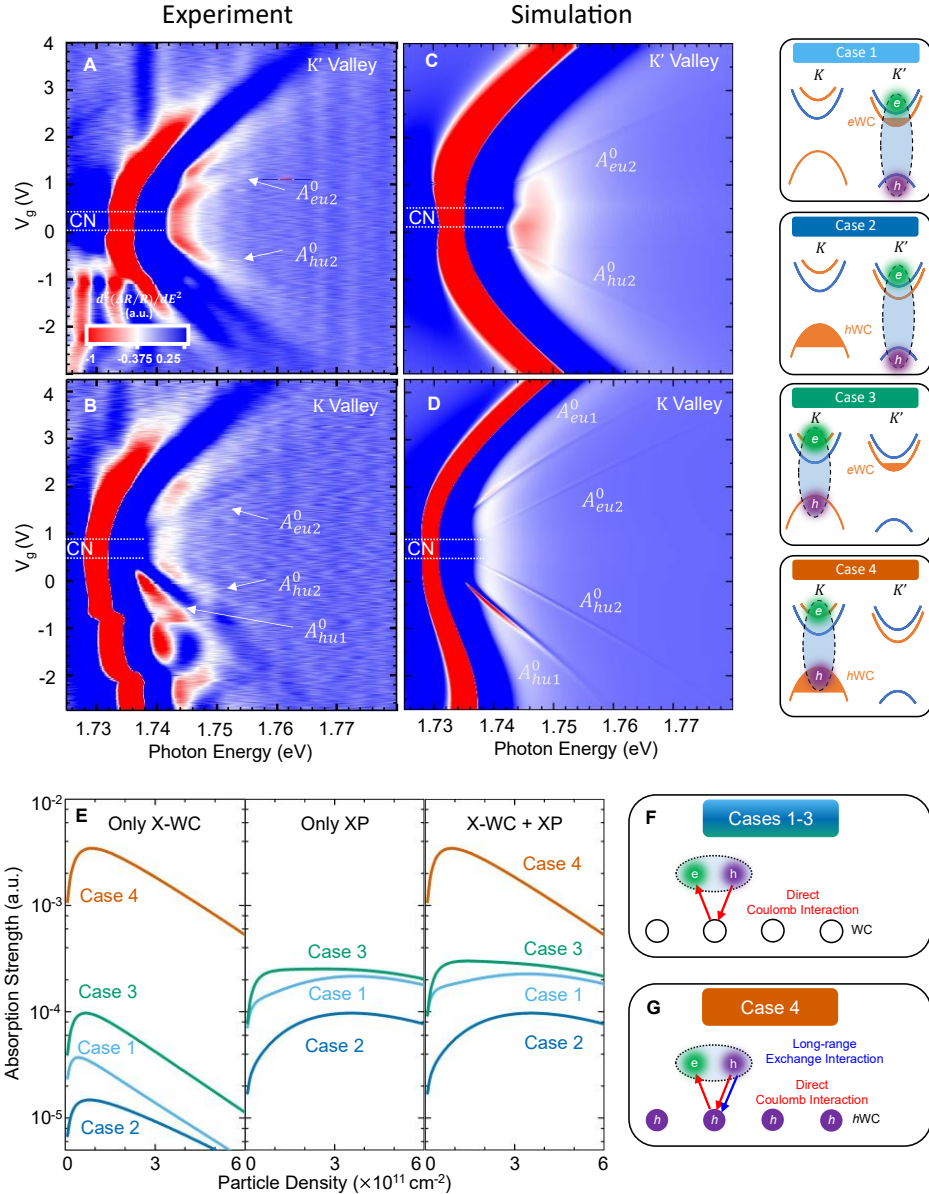


**Figure 3. Valley dependence of Umklapp scattering.** (A) Second-derivative reflectance contrast map,  $d^2(\Delta R/R)/dE^2$ , measured with left-handed circularly polarized light at a magnetic field of  $B = 17$  T, probing optical transitions in the  $K'$  valley. (B) Same as panel A, but measured with right-handed circularly polarized light, probing the  $K$  valley. (C, D) Corresponding simulated spectra for panels A and B, respectively. The simulation neglects the Landau quantization effect. The schematics on the right show the valley configurations of the exciton and the Wigner crystal, defining Cases 1–4 considered in the model. They are arranged vertically to correspond to the map sections in panels A and B. (E) Calculated oscillator strength of the Umklapp scattering signal for Cases 1–4 with only exciton–WC scattering (left), only the exciton–polaron effect (middle), and both effects included (right). (F) Schematic of exciton–WC scattering processes for Cases 1–3, in which exchange interactions are weak and direct Coulomb interactions cancel. (G) Schematic of exciton–WC scattering for Case 4, illustrating that an imbalanced exchange interaction leads to strong net scattering.

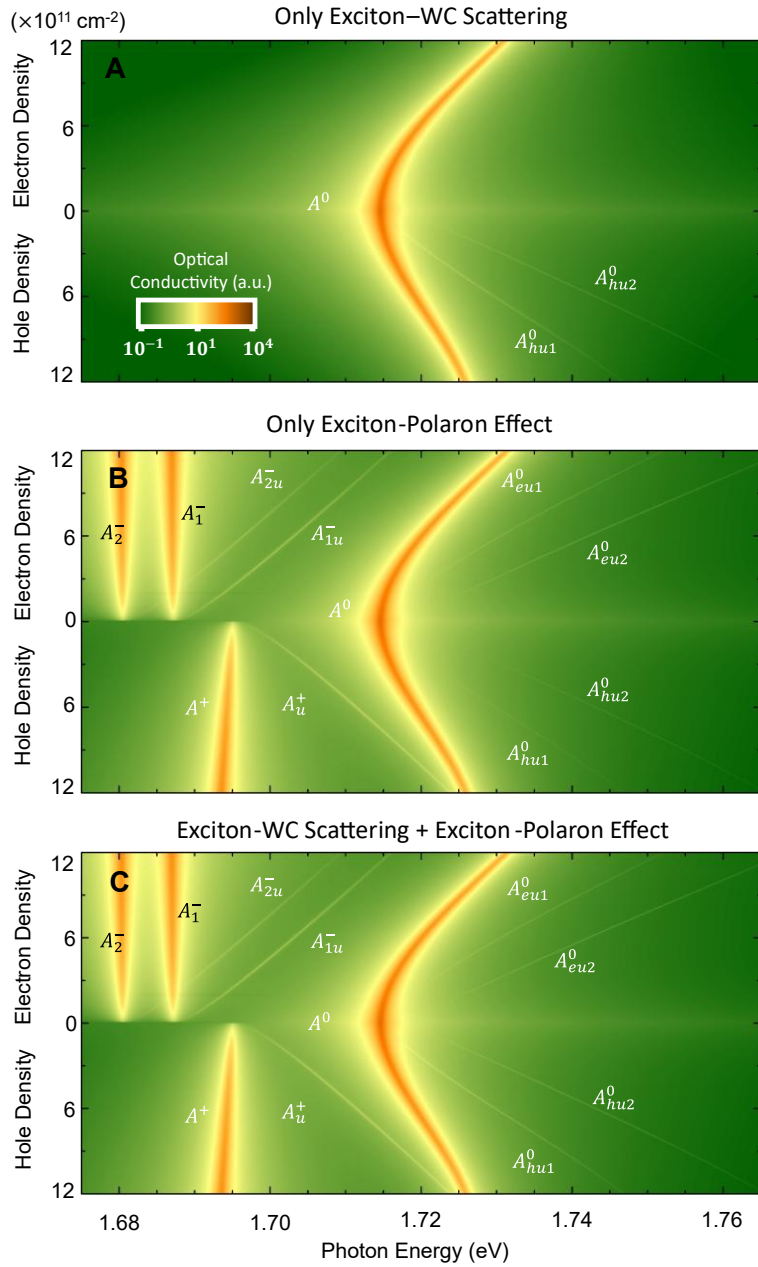


**Figure 4. Simulations of excitonic optical conductivity in monolayer WSe<sub>2</sub> Wigner crystals.** **(A)** Simulation including only exciton–WC scattering, showing Umklapp features arising from direct exciton–WC coupling. **(B)** Simulation including only exciton–polaron effects, showing the Umklapp optical response due to many–body dressing in the absence of exciton–WC scattering. **(C)** Simulation incorporating both exciton–WC scattering and exciton–polaron effects, reproducing the emergence of multiple Umklapp branches.